Remote Sensing of Atmospheric Temperature Profiles with the Nimbus 5 Microwave Spectrometer

J. W. WATERS

Jet Propulsion Laboratory, California Institute of Technology, Pasadena 91103

K. F. KUNZI,[1] R. L. PETTYJOHN, R. K. L. POON[2] AND D. H. STAELIN

Research Laboratory of Electronics, Massachusetts Institute of Technology, Cambridge 02139

(Manuscript received 22 October 1974, in revised form 12 June 1975)

ABSTRACT

This article discusses remote sensing of atmospheric temperatures with the NEMS microwave spectrometer on the Nimbus 5 satellite, and the accuracy with which atmospheric temperatures can be determined by NEMS. The sensitivity of the NEMS instrument allows measurement of temperature profiles having vertical resolution of the respective NEMS weighting functions (~10 km) with an rms accuracy of a few tenths of a degree Kelvin for a 16 s integration time. The accuracy of NEMS in estimating atmospheric temperatures at the discrete levels (~2 km vertical resolution in the lower troposphere) used in the operational numerical model of the National Meteorological Center (NMC) is ~2 K rms, as determined by comparing NEMS results with ground truth data obtained from the NMC operational analysis and from coincident radiosondes. These accuracies are consistent with the theoretical accuracies expected for NEMS.

1. Introduction

The Nimbus 5 (Nimbus E) Microwave Spectrometer experiment (NEMS) is the first application of microwave techniques for the remote sensing of atmospheric temperatures from an earth-orbiting satellite. Over oceanic areas NEMS also measures atmospheric water, both liquid and vapor. NEMS measurements can also be used to infer surface properties. A previous publication (Staelin *et al.*, 1973) has briefly discussed the experiment. A companion article (Staelin *et al.*, 1975a) describes in detail the small extent to which clouds affect the NEMS temperature measurements, and a paper is in preparation (Staelin *et al.*, 1975b) which describes atmospheric water measurements with NEMS. Aircraft measurements with the NEMS instrument have been described by Rosenkranz *et al.* (1972).

A primary objective of the NEMS experiment was to determine the accuracy with which microwave techniques from earth orbit can provide vertical temperature profiles; NEMS was not intended to provide data for operational use. The purpose of this article is to describe the accuracy of NEMS temperature profile measurements as based on comparing results obtained during its first six months of operation with independent ground-truth measurements. The development of techniques such as NEMS to measure global atmospheric temperatures is stimulated by the need in numerical weather prediction for precise global measurements of the three-dimensional temperature field to be used as initial boundary conditions in mathematical circulation models. The very important question of the quantitative extent to which microwave measurements can improve numerical weather prediction must await their use in numerical circulation models, and is outside the scope of this article. The usefulness of the NEMS measurements can be indicated, however, by comparing their accuracy with the magnitude of the variations in the atmospheric temperature, and is done here. Since the amount of variation in the temperature profile depends upon the size, location, and season of the region being considered, considerable statistical data describing both the *a priori* temperature variation and the NEMS accuracies for different locations and seasons are presented below.

In order to provide perspective for NEMS, we here briefly summarize the development of satellite temperature sensing experiments, which has been an active area of research over the past several years. For a more detailed review of remote sensing from spacecraft, the reader is referred to the article by Houghton and Taylor (1973).

Determination of atmospheric temperature structure by satellite measurements of atmospheric thermal emission was first suggested by King (1956). King pointed out that the angular distribution of the intensity of radiation emerging from the atmosphere is the

[1] Present affiliation: Institute of Applied Physics, University of Berne, Switzerland.

[2] Present affiliation: Department of Electronics, Chinese University of Hong Kong.

Laplace transform of the Planck intensity distribution as a function of optical depth in the atmosphere, and showed that the atmospheric temperature profile could be determined from satellite measurements of atmospheric emission as a function of observation angle. Kaplan (1959) advanced the concepts of remote sensing by showing that the atmospheric temperature profile could be determined from the spectral distribution of the atmospheric emission; observations in more transparent regions of the spectrum sense deeper into the atmosphere than do observations in more opaque spectral regions. A requirement for remote sensing of atmospheric temperatures by measurements of thermal emission is that the observed thermal emission originate from a gas of known, and preferably uniform, relative abundance; otherwise, the uncertainty in abundance of the gas will make ambiguous the determination of temperature from the measurements. In the earth's atmosphere two gases having known uniform abundance for altitudes below approximately 100 km also have emission bands in spectral regions that are convenient for measurement. Carbon dioxide, a minor constituent with a relative volume abundance of 0.003, has infrared vibrational bands. Oxygen, a major constituent with a relative volume abundance of 0.21, has a microwave spin-rotational band. Prior to NEMS, all satellite experiments for remotely sensing atmospheric temperatures for meteorological purposes utilized the 15 μm wavelength CO_2 infrared band.

TIROS 7, launched December 1963, carried a Medium Resolution Infrared Radiometer (MRIR) with a rather broad channel in the 15 μm CO_2 band, which was sensitive to temperatures in the lower stratosphere and provided the first satellite measurements of atmospheric temperatures (Kennedy and Nordberg, 1967). The Satellite Infrared Spectrometer (SIRS), a grating spectrometer, flown on Nimbus 3, launched April 1969, and on Nimbus 4, launched April 1970, contained seven channels in the 15 μm band, which sensed temperatures in seven layers of the troposphere and lower stratosphere (Wark and Hilleary, 1969; Smith *et al.*, 1970; Smith *et al.*, 1972b). Nimbus 3 and Nimbus 4 also carried an Infrared Interferometer Spectrometer (IRIS) that measured atmospheric radiation from 400 to 2000 cm^{-1} with 5 cm^{-1} spectral resolution on Nimbus 3, and from 400 to 1600 cm^{-1} with 2.8 cm^{-1} resolution on Nimbus 4 (Hanel *et al.*, 1970, 1971). Also on Nimbus 4 was the Selective Chopper Radiometer (SCR), which used cells of CO_2 as filters to provide significantly improved spectral resolution over previous experiments and sensed temperatures well into the upper stratosphere (Barnett *et al.*, 1972). The first satellite experiment to measure atmospheric temperatures for operational meteorological use is the Vertical Temperature Profile Radiometer (VTPR) on NOAA 2, launched in October 1972 (Jastrow and Halem, 1973). Nimbus 5, launched 11 December 1972, carried an advanced 16-channel selective chopper radiometer (Houghton and Smith, 1972), and a 7-channel Infrared Temperature Profile Radiometer (ITPR) (Smith *et al.*, 1972a) with a very narrow scanning field of view for observing radiation from clear areas in partially overcast conditions and providing temperature profiles for such areas.

The determination of atmospheric temperatures from satellite measurements of thermal microwave emission by atmospheric oxygen was first suggested by Meeks (1961). Meeks and Lilley (1963) developed the basic concepts for sensing atmospheric temperatures and performed the first calculations of microwave temperature weighting functions describing the altitude layers sensed by microwaves. Lenoir (1968) extended the theory of Meeks and Lilley to the upper stratosphere and mesosphere where the earth's magnetic field makes the oxygen emission, which is due to magnetic dipole transitions, both polarized and anisotropic. During the ten years between the work of Meeks and Lilley and the launch of Nimbus 5, several experiments have measured atmospheric oxygen emission from the ground (Westwater, 1972; Miner *et al.*, 1972; Waters, 1973), from balloon (Barrett *et al.*, 1966; Lenoir *et al.*, 1968) and from aircraft (Rosenkranz *et al.*, 1972) for determining atmospheric temperatures. Staelin (1969) and Tomiyasu (1974) reviewed microwave remote sensing techniques.

The primary advantage of microwave over infrared temperature sounders is that the longer wavelength microwaves are much less affected by clouds and precipitation than the shorter infrared wavelengths, and can be used to determine atmospheric temperatures in overcast conditions. At best, sophisticated techniques are required to eliminate the effects of clouds on the infrared measurements. Several such techniques have been developed (Smith *et al.*, 1970; Rodgers, 1970; Chahine, 1970, 1974), none of which are valid under all conditions encountered in the atmosphere, for example, complete overcast.

All the results presented in this paper were obtained with the simplest possible correction for cloudiness; the effects of clouds on the NEMS measurements were simply ignored. A quantitative discussion of the effects of clouds on NEMS temperature sounding is given in the accompanying article by Staelin *et al.* (1975a).

2. Atmospheric oxygen emission

The oxygen molecule has a magnetic dipole moment arising from the combined spins of two unpaired electrons in its $^3\Sigma_g^-$ electronic ground state. Changes in the orientation of this electronic spin, relative to the orientation of the molecular rotation, produce a band of magnetic dipole transitions near 60 GHz (5 mm wavelength) and a single transition at 118 GHz (2.5 mm wavelength). These transitions make possible microwave sensing of atmospheric temperatures.

Van Vleck (1947) first derived the expressions for calculating microwave absorption of O_2 by summing absorption of the individual spin-rotation transitions. It was found by several workers (Artman and Gordon, 1954; Crawford and Hogg, 1956; Straiton and Tolbert, 1960), however, that if the linewidth parameter measured at low pressures where the individual lines are resolved is assumed proportional to pressure and used in Van Vleck's expression, the calculated absorption on the wings of the 60 GHz band for 1 atm pressure is significantly higher than measured values. For atmospheric calculations, it has been common practice to correct this discrepancy in the calculations by making the linewidth parameter an empirical function of pressure, or of altitude, such that the calculated absorption agrees with measurement (Meeks and Lilley, 1963; Barrett *et al.*, 1966; Carter *et al.*, 1968; Reber, 1972). It should be noted that the discrepancy exists whether one uses the Van Vleck-Weisskopf shape for individual lines, as was done originally by Van Vleck, or the kinetic line shape later derived independently by Gross (1955) and Zhevakin and Naumov (1963). The origin of the discrepancy is probably due to coherence effects between overlapping lines that are not accounted for by the Van Vleck expression. Gordon (1967) has studied the problem of overlapping spin-rotation lines in pure O_2 and developed a theory that predicts that collisions become less effective in broadening the O_2 band when the pressure becomes so large that there is significant overlapping, which occurs at pressures above approximately 50 mb. Rosenkranz (1975) has recently developed a first-order expansion of Gordon's theory which is amenable to atmospheric calculations, but the Rosenkranz expressions were not available at the time the analysis described in this article was performed.

For our theoretical calculations of atmospheric emission to compare with NEMS measurements, the Van Vleck expression with the kinetic line shape for individual microwave transitions was used. The empirical line width obtained by Reber (1972) was used for all transitions except the isolated 118 GHz line. For this line, which is not overlapped by other lines, we used a linewidth parameter proportional to pressure with the proportionality constant determined from measurements (Schulze and Tolbert, 1963).

At microwave frequencies and for the range of temperatures encountered in the earth's atmosphere, the Planck source function is proportional to temperature within an excellent approximation. The radiative transfer equation describing the intensity of radiation emerging from the atmosphere can then be written in terms of the brightness (equivalent blackbody) temperature of the radiation:

$$T_B(\nu)=\int_0^\infty T(z)e^{-\tau_\nu(z,\infty)}k_\nu(z)dz + R\exp(-\tau_\nu^0)\int_0^\infty T(z)e^{-\tau_\nu(0,z)}k_\nu(z)dz + (1-R)T_s\exp(-\tau_\nu^0), \quad (1)$$

where $T_B(\nu)$ is the brightness temperature at frequency ν of the emergent radiation, $\tau_\nu(z_1,z_2)$ the optical depth between altitudes z_1 and z_2, τ_ν^0 the optical depth through the entire atmosphere, $k_\nu(z)$ the absorption coefficient at frequency ν and altitude z, $T(z)$ the temperature at altitude z, R the surface reflectivity, and T_s surface temperature. Note that τ_ν here denotes optical depth and not transmissivity [given by $\exp(-\tau_\nu)$], as is commonly the case in infrared work. The three terms on the right side of (1) represent, respectively (i) upward emission by the atmosphere, (ii) downward emission by the atmosphere that is reflected by the surface and attenuated in its upwelling path by the intervening atmosphere, and (iii) emission by the surface attenuated by the intervening atmosphere.

NEMS channels 3, 4 and 5 are centered at frequencies 53.65, 54.90 and 58.80 GHz in the oxygen band and sense atmospheric temperatures in the troposphere and lower stratosphere. Approximate values of total zenith atmospheric opacity τ_ν^0 at these frequencies are 2, 6 and 30, respectively, corresponding to transmissivities of 0.14, 2.5×10^{-3} and 10^{-13}. Ocean surface reflectivities are typically 0.5 and land surface reflectivities are typically 0.05 for these frequencies. Surface effects produce negligible effect on channels 4 and 5, and in the most extreme case produce a change of 5 K in channel 3 when Nimbus 5 crosses a land-water boundary.

Neglecting reflection and emission by the surface, (1) reduces to

$$T_B(\nu)=\int_0^\infty T(z)e^{-\tau_\nu(z,\infty)}k_\nu(z)dz. \quad (2)$$

The factor multiplying $T(z)$ in the integrand of (2) is, by definition, the temperature weighting function. Since NEMS measures radiation over a frequency interval $\Delta\nu$ covering 0.010 to 0.110 GHz either side of the center frequency of each channel, (2) must be integrated over this frequency interval to give the brightness temperature measured by NEMS for that channel. This gives for the weighting function

$$W=\int_{\Delta\nu} e^{-\tau_\nu(z,\infty)}k_\nu(z)d\nu. \quad (3)$$

Fig. 1 gives weighting functions calculated for the NEMS temperature sounding channels. Below, we

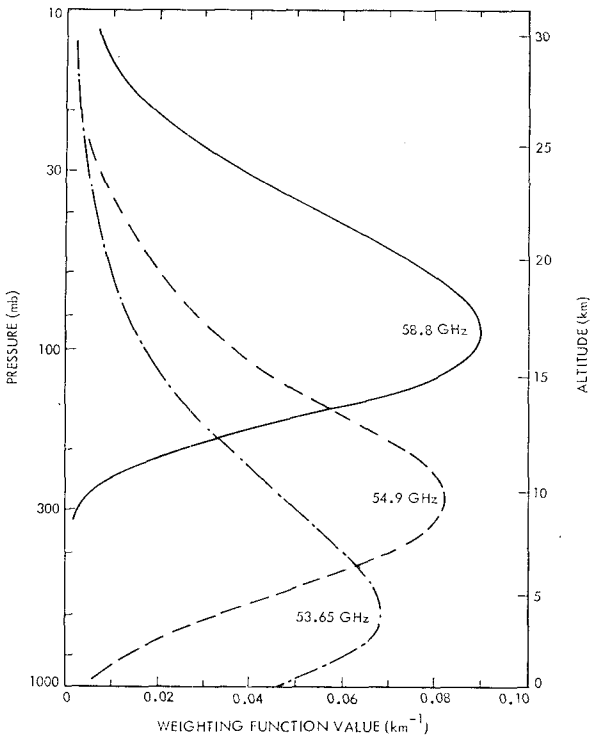

FIG. 1. NEMS temperature weighting functions calculated for the 1962 U. S. Standard Atmosphere and zero surface reflectivity.

discuss some implications of the NEMS measurements on the weighting functions.

3. NEMS measurements

Each NEMS channel measures atmospheric radiation collected by a 10° beamwidth (full width at half-power points) nadir-looking antenna. This beamwidth produces a resolution element of approximately 200 km diameter along the sub-satellite point. The velocity of the Nimbus 5 sub-satellite point is 6 km s^{-1}. Integration time for the NEMS instrument is 2 s, but during ground data processing the measurements are integrated for 16 s, which gives an effective resolution cell having dimensions of approximately 200 km by 300 km. The rms instrumental noise for the 16 s integration time is approximately 0.1 K.

Fig. 2 shows NEMS temperature channel measurements for a portion of an orbit in December 1972 passing over the tropical Pacific. Each point in Fig. 2 represents an independent 16 s integration period. The 0.1 K rms sensitivity of the instrument for this integration time is evident from the small scatter in these points, and it can be seen that brightness temperature changes of a fraction of a degree can be readily measured. The climatological features of the tropical tropospheric temperature structure are also evident in Fig. 2. Channel 3 is most sensitive to the lower troposphere, which is warmer toward the equator and colder toward the poles. Channel 5 is most sensitive to temperatures near 17 km altitude where coldest temperatures occur near the equator. Channel 4 senses the upper troposphere, which exhibits smaller temperature variation with latitude than either the lower troposphere or tropopause. The cold depressions in channel 3 indicated by arrows labeled ITCZ are due to clouds and precipitation in the intertropical convergence zone, and illustrate the small effects of clouds on the NEMS measurements.

For comparison with calculations of atmospheric emission, and for determining atmospheric temperature profiles, the NEMS measurements are first corrected for the approximately 4% of total energy received by the antennas from outside the main beam. This correction to the measurement amounts to approximately 5 K and is precomputed as a function of latitude from climatic variations in atmospheric temperature. The remaining uncertainty, other than a constant offset which is eliminated as discussed in Section 5, is estimated to be 0.3 K rms.

4. Atmospheric comparison data

Two sets of atmospheric data are routinely compared with NEMS data: 1) data from selected radio-

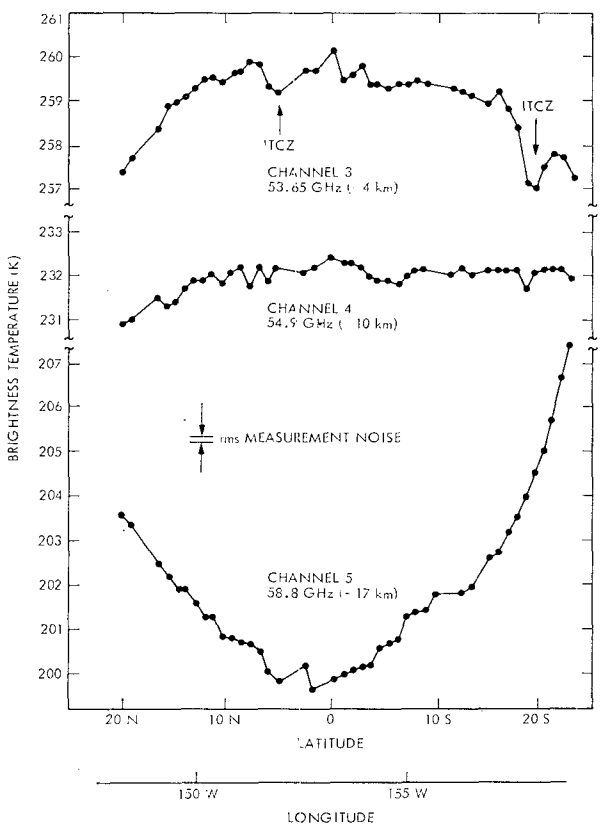

FIG. 2. Brightness measurements of the NEMS temperature sounding channels illustrating the precision of measurements and small effects of extensive cloudy regions in the intertropical convergence zone (ITCZ) on channel 3.

TABLE 1. Nimbus 5 coincident radiosondes used for NEMS comparisons.

Station	Latitude (deg)	West longitude (deg)	Number of coincident radiosondes Dec 72	Jan 73	Feb 73	Mar 73	Apr 73	June 73	Aug 73	Station totals
Poker Flats	65.01	147.48		5	3	1				9
Fort Churchill	58.73	93.82	1	4		2	3	2	2	14
Primrose Lake	54.75	110.05		1			1			2
Wallops Island	37.85	75.48		1	2	1	2			6
Point Mugu	34.12	119.12	2	4	6		1			13
White Sands	32.38	106.48		4	5	2	1	3		15
Cape Kennedy	28.45	80.53						1		1
Barking Sands	22.03	159.78	1	3	5	1	2	2		14
Fort Sherman	9.37	79.95			1	1	3	3		8
Monthly totals			4	22	22	8	13	11	2	82

sondes launched coincident with Nimbus 5, and 2) interpolations in time and space from the Northern Hemisphere, octagon-shaped, 1977 element, analysis grid prepared by the National Meteorological Center (NMC). These atmospheric data are used both for calculating emission for comparison with NEMS measurements, and for comparison with atmospheric temperature profiles determined from NEMS.

During 1973 several Northern Hemisphere radiosonde and rocketsonde stations launched Nimbus 5 coincident soundings. Data from these soundings were collected by the Upper Air Branch of NMC and supplied to the Massachusetts Institute of Technology (MIT). At the time of preparation of this paper 82 of these soundings had been matched with NEMS measurements. Table 1 gives the distribution of these soundings among stations and months. The rms and maximum differences in space (Δs) and time (Δt) between the soundings and Nimbus 5 overflies are given in Table 2 for all the soundings, and individually for three stations to be considered in detail below. For computing the values of Table 2, the spatial distance between Nimbus 5 and the sounding was defined as the distance of closest approach of the sub-satellite point to the station location. The time difference was defined as the difference between time of launch of the sounding and the time at which Nimbus 5 was at closest approach to the station. It should be noted that the rms time differences are of the same order as the duration of a radiosonde measurement.

The NMC Northern Hemisphere analysis grid is prepared from data obtained from radiosondes launched daily at synoptic times of 0000 and 1200 GMT, data obtained from the commercial aircraft flights, and measurements over oceanic areas from the Vertical Temperature Profile Radiometer on the NOAA 2 satellite. The boundary of the NMC grid is shown as a dashed line in Fig. 3. The different regions indicated in Fig. 3 were used for NEMS analysis and will be discussed later. Meteorological data at the NMC grid points include temperature at pressure levels of 1000, 850, 700, 500, 400, 300, 250, 200, 150 and 100 mb. Stratospheric temperature data at pressure levels of 70, 50, 30 and 10 mb are also generated by NMC for the grid points, but only once daily at 0000 GMT. To compare NEMS-determined temperature profiles with NMC profiles, atmospheric temperatures at these standard NMC pressure levels were routinely determined from NEMS measurements by the procedure discussed in Section 6. For comparison with NEMS measurements at a particular time and location, the four grid points surrounding the NEMS location are first located. Values from these grid points are bilinearly interpolated to the NEMS location for the two NMC grid times either side of the NEMS measurement time. These two spatially interpolated values are then interpolated in time to the NEMS measurement time for comparison with NEMS.

5. Comparison between calculated and measured atmospheric emission

Before atmospheric temperatures were determined from large quantities of NEMS measurements, the measurements were first compared with calculations of atmospheric emission. This comparison gives insights into the accuracy of the oxygen absorption coefficient expressions, and is used for determining the required modifications of theory or measurements to provide consistency between the two.

Atmospheric emission was calculated using the comparison atmospheric data discussed above in the ra-

TABLE 2. Time and spatial distances between coincident radiosondes and Nimbus 5.

Station	Δs (km) rms	Δs (km) maximum	Δt (min) rms	Δt (min) maximum
All ($N=82$)	118	450	46	180
Fort Churchill ($N=14$)	79	262	45	130
White Sands ($N=15$)	108	410	73	180
Barking Sands ($N=14$)	123	448	30	84

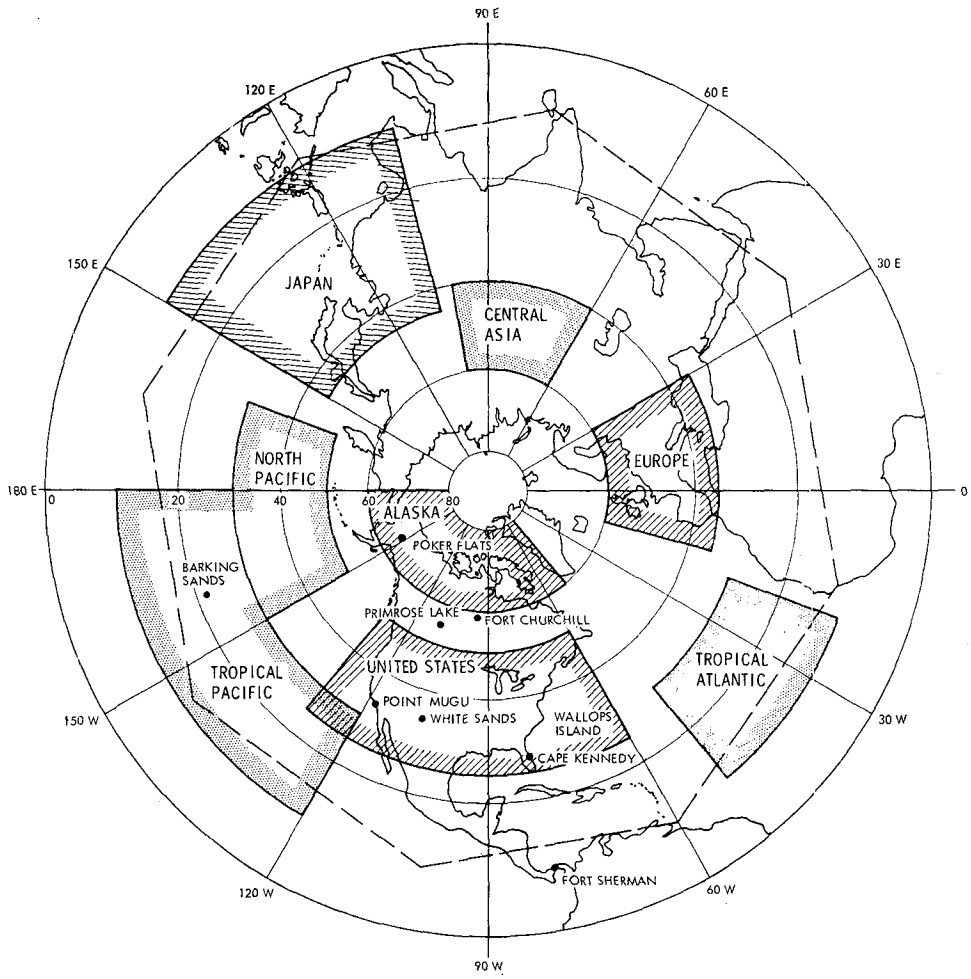

FIG. 3. Northern Hemisphere map showing regions used for comparing NEMS and interpolated NMC grid temperature profiles. Boundaries of the octagon-shaped NMC grid are shown as dashed lines. Locations of radiosonde stations launching Nimbus 5 concident soundings are also shown.

diative transfer equation (1). The calculated brightness temperature was integrated over the bandwidths of individual NEMS channels by using an equivalent frequency for each channel, such that the monochromatic calculation at the equivalent frequency equals the calculated emission integrated over the channel bandwidth. This procedure of obtaining brightness temperatures integrated over the channel bandwidths greatly reduced the required computation effort; over the extremes of conditions encountered in the atmosphere it produced an additional error of at most a few tenths of a degree in the calculated brightness temperature. Equivalent frequencies of 53.647, 54.943 and 58.875 GHz were determined for channels 3, 4 and 5, respectively.

In addition to the temperature profile, obtained from the comparison atmospheric data, the calculation of atmospheric emission for channel 3, which is slightly affected by the surface, requires knowledge of the surface temperature and reflectivity. For the surface temperature T_s we used the atmospheric temperature at 1000 mb from the comparison data. The surface reflectivity was determined from NEMS channel 1 and 2 measurements (at 22.235 and 31.4 GHz, respectively), as follows.

The surface reflectivity for channel 2 can be well approximated by the expression

$$R_2=\frac{(T_{B2}-T_{e2})+(T_{e2}-T_s)\exp(-\tau_2^0)}{\{T_{e2}[1-\exp(-\tau_2^0)]-T_s\}\exp(-\tau_2^0)}, \quad (4)$$

where T_{B2} is the measured brightness temperature for channel 2, and T_{e2} an equivalent atmospheric emission temperature for channel 2, which we found from regression analysis of simulated data could be given by

$$T_{e2}=0.965\times T(850\text{ mb}), \quad (5)$$

where $T(850\text{ mb})$ is the atmospheric temperature at 850 mb pressure level.

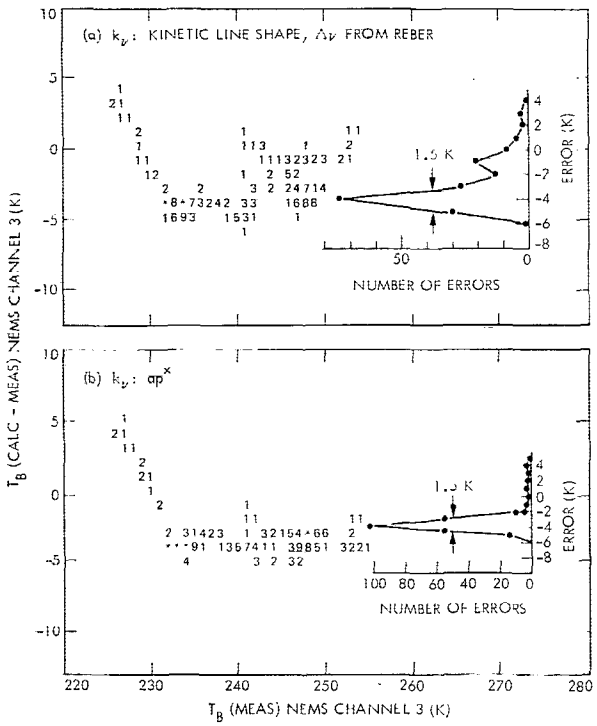

FIG. 4. Comparison of calculated and measured brightness temperatures for NEMS channel 3.

The atmospheric transmissivity for channel 2, $\exp(-\tau_2^0)$ is required in (4) for the reflectivity and can also be determined from channel 1 and 2 measurements if the relation between the opacities and between surface reflectivities for these channels are known or can be estimated. Calculations on atmospheric data yielded the regression equation

$$\exp(-\tau_2^0)=a\exp(-\tau_1^0)+b, \tag{6}$$

where $a=0.32$ and $b=0.66$. The relation between the surface reflectivities for channels 1 and 2 was assumed to be

$$\frac{R_2}{R_1}=r, \tag{7}$$

where a value of 0.94 corresponding to flat sea water was used for r when Nimbus 5 was over ocean and a value of 1.0 when it was over land. With (6) and (7), and making the approximation that the equivalent atmospheric emission temperature equals the surface temperature, which is valid to within $\sim 5\%$ and adequate for obtaining $\exp(-\tau_2^0)$ to the accuracy required for (4), the atmospheric transmissivity for channel 2 can be written

$$\exp(-\tau_2^0)=b\left[1-a\left(r\frac{T_s-T_{B1}}{T_s-T_{B2}}\right)^{\frac{1}{2}}\right]^{-1}, \tag{8}$$

where T_{B1} is the measured brightness temperature in channel 1. Eq. (5) can then be used in (4) and a reflectivity for channel 2 obtained. The reflectivity for channel 3 is then taken to be

$$R_3=0.88R_2, \tag{9}$$

as this is the relation expected for flat ocean water. It also gives sufficient accuracy for channel 3 reflectivities over land, as then the reflectivities are very close to zero.

With the above expressions and the comparison atmospheric data, brightness temperatures corresponding to the NEMS measurements can be calculated and compared with the actual measured values. When we performed such calculations, the effects of water vapor on the oxygen channels were included by using water vapor values also given in the comparison atmospheric data set, and the water vapor absorption coefficient as expressed by Staelin (1966).

Comparisons of calculated and measured emission of the NEMS temperature sounding channels are shown in Figs. 4–6. The horizontal axes of these figures give the value of the measured brightness temperature; the vertical axes give the discrepancy, defined as calculated minus measured, between the calculation and measurement. The digits in each figure represent the number of times a given discrepancy occurred, and asterisks denote numbers larger than 9. An inset in each figure shows the distribution of dis-

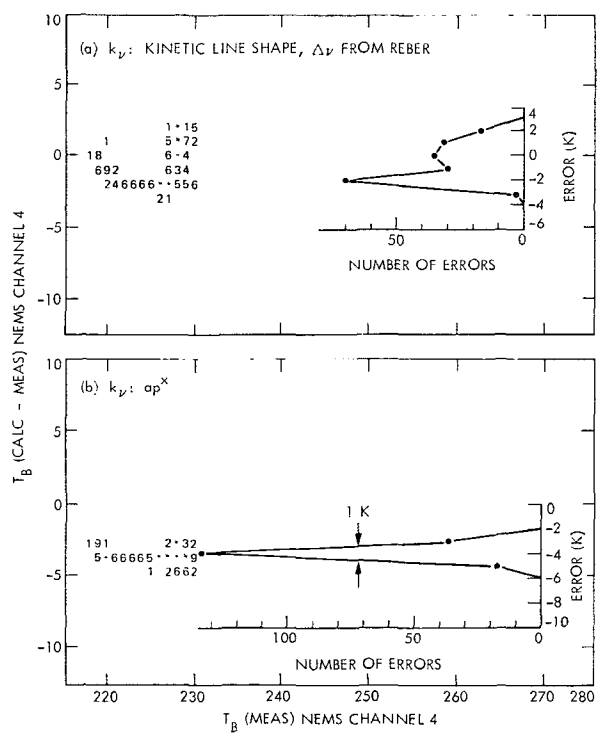

FIG. 5. Comparison of calculated and measured brightness temperatures for NEMS channel 4.

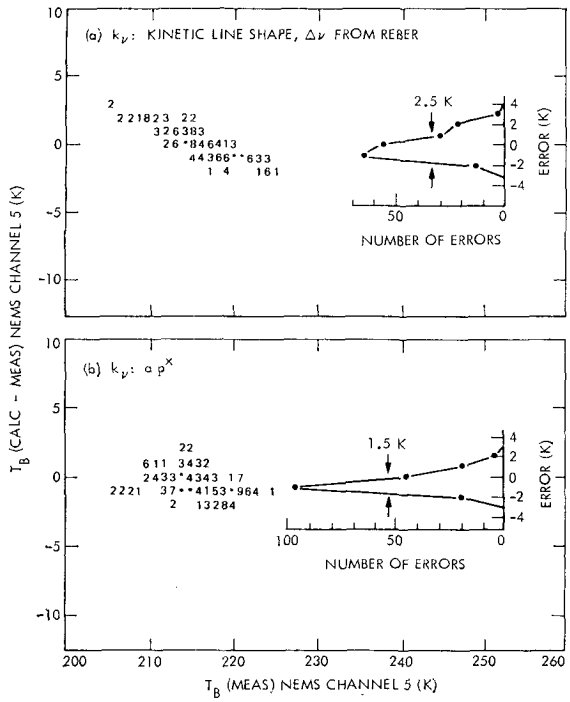

FIG. 6. Comparison of calculated and measured brightness temperatures for NEMS channel 5.

crepancies ("errors"). The top portion of each figure was obtained with calculations using the theoretical oxygen absorption coefficient with the kinetic line shape for the individual O_2 transitions, and the empirical linewidth parameter of Reber (1972). The bottom portion of each figure was obtained with calculation using an absorption coefficient of the form $k_\nu = ap^x$ where a and x are determined empirically to minimize the spread in the distribution of discrepancies. The values used for a and x are given in Table 3.

The results shown in Figs. 4–6 represent data from a single day, 18 February 1973. The significance of this particular date is that it occurred during the first week for which we obtained sufficient atmospheric comparison data to perform the calculations. The atmospheric data used for the calculations were obtained from selected regions of the NMC grid labeled as UNITED STATES, EUROPE, JAPAN and ALASKA in Fig. 3. These regions were chosen to eliminate areas of more questionable accuracy in the NMC grid, and yet still provide data from various climates. NEMS brightness temperatures were obtained for every 16 s interval during which Nimbus 5 was in the selected regions. Also, for each of these 16 s intervals, data from the NMC grid were interpolated in time and space to the sub-satellite point. These interpolated NMC data were used to calculate NEMS brightness temperatures, as described above. The difference between calculation and measurement were then plotted as a function of the measured value to produce Figs. 4–6.

TABLE 3. Values of a and x for oxygen absorption coefficient and brightness temperature offsets empirically determined for NEMS temperature sounding channels.

Channel	a	x	T_B offset (K)
3	1.60×10^{-5}	1.5	−3.3
4	1.42×10^{-5}	1.75	−3.9
5	1.26×10^{-8}	4.0	−0.7

A first thing to note in the comparison of calculated and measured brightness temperatures is the amount of offset between the peak of the error distributions and zero. These offsets are given in Table 3 and indicate the discrepancy in our calculation and measurement of the absolute value of brightness temperature for the NEMS channels. For the worst case, channel 4, this discrepancy is 1.7% of the total absolute value, and includes any bias in the NMC grid and the interpolation process for obtaining the comparison atmospheric data, as well as any effects of clouds or rain, which were not included in the calculations since no comparison atmospheric data existed for condensed water. The absolute calibration of the NEMS instrument is believed to be 1% or better, and these comparisons indicate this to be true, since approximately half (or ~1%) of the discrepancy between calculation and measurement is believed due to uncertainties in the calculation.

As we could not easily determine the source of these small offsets, it was assumed due to the instrumental calibration and of an additive nature. Consequently, these offsets were subtracted from the measured brightness temperatures before atmospheric temperatures were determined from the NEMS data, as will be described later.

A second thing to note from the comparisons is that the empirical oxygen absorption coefficient ap^x significantly decreases the spread in the error distribution over the "theoretical" absorption coefficient calculation. (The "tail" at low measured brightness temperatures on channel 3 results from high-altitude surface effects, which were not removed before producing the plot for channel 3.) This has implications for the physics of atmospheric oxygen absorption, which we plan to discuss in more detail in a later paper. We shall point out here, however, that there is a significant slope that exists in the discrepancy versus measured value for the theoretical absorption coefficient calculation for channel 5. A value $x=4$ in the empirical ap^x absorption coefficient eliminates this slope. The theoretical expressions for the oxygen expression predict values of x approximately equal to 2. The numerical value of x is of interest because the width of the weighting function is inversely proportional to x. If x is closer to 4 than to 2 for channel 5,

the weighting function for this channel is sharper by a factor of approximately 2 than that given by the theoretical weighting function shown in Fig. 1. To further test this behavior in channel 5, we performed calculations on the coincident radiosonde data and obtained similar results. The calculations from the radiosonde data further supported a sharper weighting function for channel 5 than theoretically calculated; it was found that the calculation and measurement agreed quite closely (to better than ~1 K) for arctic cases where the temperature structure is relatively isothermal over the altitude region sensed by channel 5, but that in the tropics the measured brightness temperatures were significantly (~4 K) colder than those calculated from the theoretical absorption coefficient. Since the peak of the channel 5 weighting function occurs very near the cold tropical tropopause, the only way that measured values could be colder than calculated values is if the actual weighting function is sharper than calculated. The fact that calculation and measurement agree closely in the more isothermal arctic case indicates calibration of the instrument is accurate, because an isothermal profile gives the same brightness temperature for any absorption coefficient, and can be used to check the instrument calibration.

One expects the theoretical expressions used here for the oxygen absorption coefficient to be less accurrate in pressure regions where the individual oxygen lines begin to overlap, and it is just this pressure region that channel 5 senses. Thus, we suspect overlapping line effects produce the channel 5 behavior, but we cannot be conclusive on this point because preliminary laboratory measurements have failed to verify this behavior (Poon, 1974; Liebe, 1975).[3]

It must be noted that the ap^x absorption coefficient expressions obtained here apply, of course, only over the pressure regions to which the respective NEMS channels are sensitive.

6. Determination of atmospheric temperature profiles from NEMS measurements

The accuracy of NEMS in determining atmospheric temperature profiles with the vertical resolution of the individual NEMS weighting functions is a few tenths of a degree Kelvin for a 16 s integration as indicated by the measurements of Fig. 2. However, numerical models which are presently used for weather forecasting require vertical temperature resolution much better than that given by the weighting functions. For example, the NMC operational numerical model utilizes temperatures at 14 discrete pressure levels, as described in Section 4. We have elected, therefore, to evaluate the accuracy with which NEMS can infer atmospheric temperatures at the lower 13 NMC levels which are within the vertical region sensed by NEMS, since we felt such knowledge would be useful for evaluating the potential of NEMS for operational use. We have further elected to use the rms discrepancy between NEMS results and the comparison atmospheric data for describing the NEMS accuracy, as this is probably the most meaningful indicator of the accuracy, and also as this has been common practice in remote sensing experiments.

Temperatures at discrete levels (or layers) can be estimated from the NEMS measurements because these temperatures are correlated with the temperature over the weighting function layer, which is measured. Since the correlation is not perfect, the inference of temperatures at discrete levels from NEMS is less accurate than the inference of an averaged temperature over the weighting function layer. Several techniques have been developed for the determination of atmospheric temperature profiles from radiance measurements. These include the methods of Rodgers (1966), Westwater and Strand (1968), and Smith *et al.* (1970), which use statistical information of the temperature profile. Such methods are reviewed by Rodgers (1971), and similar methods have been developed and used by Soviet workers (for example, Malkevich *et al.*, 1969; Pokrovsky and Timofeyev, 1972). Conrath (1972) has applied the Backus-Gilbert technique, which relates resolution and accuracy, to atmospheric temperature sensing. Chahine (1968, 1970, 1972, 1974) has developed relaxation methods which do not require statistical information.

The method used here for obtaining temperature profiles from NEMS measurements is essentially a regression analysis of atmospheric temperature profiles and numerically-calculated atmospheric emission, and is similar to the statistical methods mentioned above. The atmospheric temperature is represented by the vector $\mathbf{T}$ whose elements give the temperature at discrete altitudes. This temperature vector is assumed related to a vector function of the NEMS measurements $\phi(T_B)$ by a matrix $\mathbf{D}$:

$$\mathbf{T}=\mathbf{D}\cdot\phi(T_B). \tag{10}$$

The measurement basis function vector we used for determining atmospheric temperatures is

$$\phi(T_B)=\begin{bmatrix} 1 \\ T_{B3}-\bar{T}_{B3} \\ T_{B4}-\bar{T}_{B4} \\ T_{B5}-\bar{T}_{B5} \\ (T_{B3}^2-\bar{T}_{B3}^2)/\bar{T}_{B3}^2 \\ (T_{B4}^2-\bar{T}_{B4}^2)/\bar{T}_{B4}^2 \\ (T_{B5}^2-\bar{T}_{B5}^2)/\bar{T}_{B5}^2 \end{bmatrix}, \tag{11}$$

where T_{Bn} is the brightness temperature for NEMS channel n and an overbar indicates expected value. Although nonlinear terms were included in the measurement basis function vector, as indicated above, they were found to contribute a negligible amount to

[3] H. J. Liebe, Office of Telecommunications, U. S. Dept. of Commerce, private communication.

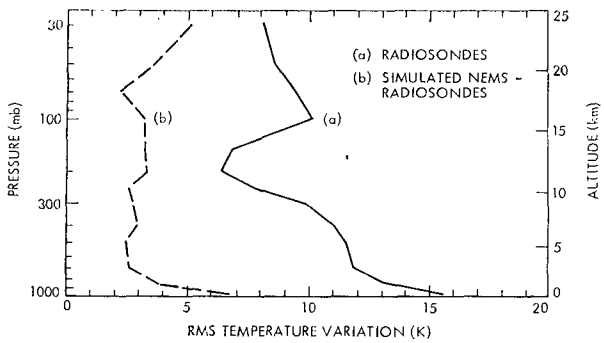

FIG. 7. Theoretical accuracy of determining atmospheric temperature profiles from NEMS measurements. Curve (a) gives the rms variation in the radiosonde data, and curve (b) shows the rms discrepancy between the simulated NEMS experiment and the radiosondes. Approximately 400 radiosondes were used for the simulation.

the inferred temperature vector. The inferred temperature vector $\mathbf{T}$ was chosen to have elements corresponding to the discrete pressure levels used in the NMC grid. Values for these pressure levels have been given above in the description of the comparison atmospheric data. The matrix $\mathbf{D}$ is chosen to minimize the expected error between the NEMS-determined profile and the actual temperature profile, and is given by

$$\mathbf{D}=\mathbf{C}(\mathbf{T},\phi)\mathbf{C}^{-1}(\phi,\phi), \tag{12}$$

where $\mathbf{C}$ is a correlation matrix whose ijth element is

$$C_{ij}(\mathbf{x},\mathbf{y})=\overline{\mathbf{x}_i\mathbf{y}_j}. \tag{13}$$

The C_{ij} can be calculated from atmospheric statistics. A problem arises when $\mathbf{C}(\phi,\phi)$ is singular, or nearly singular, because then its inverse, which appears in (12), is undefined. The singularity problem was avoided in our calculations by including simulated measurement noise of 0.2 K in T_{Bn} which adds diagonal components to $\mathbf{C}(\phi,\phi)$ and reduces its singularity. This method of handling singularities is similar to that of Twomey (1965). An alternate method is to diagonalize $\mathbf{C}(\phi,\phi)$ and discard the eigenvectors having eigenvalues below a noise threshold. Pokrovsky (1972) has compared these methods for reducing the effects of singularities.

Computation of $\mathbf{D}$ requires the cross-correlation matrix of atmospheric temperatures and measurement basis functions, $\mathbf{C}(\mathbf{T},\phi)$, and the self-correlation matrix of measurement basis functions, $\mathbf{C}(\phi,\phi)$. These matrices were evaluated from *a priori* atmospheric data obtained from Northern Hemisphere radiosonde stations. We purposely avoided using the comparison atmospheric data in the calculation of $\mathbf{D}$ to eliminate any possibility of inbreeding the results, since the comparison data are used for evaluating the accuracy of the determined profiles. All the temperature profile results presented in this paper were obtained from a $\mathbf{D}$ matrix that was computed using only December 1960 and 1961 radiosonde data. December was chosen because Nimbus 5 was launched in December; we initially planned to calculate a $\mathbf{D}$ matrix for each season, but this has not been done for the results presented here. Neither were $\mathbf{D}$ matrices for separate climatological regions used to obtain these results; rather, a "global" $\mathbf{D}$ was used for all regions.

Although a single $\mathbf{D}$ is used here for all climates and seasons, different $\mathbf{D}$'s are used depending on whether Nimbus 5 is over land, water, or a combination of the two. This procedure corrects for the slight dependence of channel 3 on surface reflectivity. In practice, nine $\mathbf{D}$'s are calculated from the *a priori* atmospheric data corresponding, respectively, to the reflectivity for ocean water, and to eight values of reflectivity ranging from 0.05 to 0.40 in steps of 0.05. If Nimbus 5 is over ocean, as determined from its latitude and longitude, the $\mathbf{D}$ for ocean water is used for temperature determinations. If Nimbus 5 is not over ocean, the surface reflectivity is determined from channels 1 and 2 by the procedure described in Section 5, where the required 1000 and 850 mb temperatures are first estimated from the temperature sounding channels using the $\mathbf{D}$ calculated for a reflectivity of 0.25. The $\mathbf{D}$ corresponding to the value of surface reflectivity nearest that determined from channels 1 and 2 is then used to give the atmospheric temperature profile for this particular measurement, with a slight correction to account for the fact that there may be a difference of as much as 0.025 between the determined surface reflectivity and that for which the $\mathbf{D}$ was calculated.

High-altitude surface effects on channel 3 were also accounted for by adjusting the channel 3 measurement to a value expected for a surface at sea level. We adjusted by adding an amount $\Delta T_B=0.768h+0.338h^2$ to channel 3, where ΔT_B is in K, and h in km and interpolated from the four nearest values of a global elevation map having 5° resolution in latitude and longitude.

Prior to the launch of Nimbus 5, the NEMS experiment was numerically simulated and predictions made of the accuracy with which atmospheric temperature profiles could be determined. The predicted accuracy is shown in Fig. 7.

7. Results

Fig. 8 shows individual temperature profiles determined from NEMS and measured by coincident radiosondes. The 18 January Poker Flats profile and the 27 June Ft. Sherman profile were chosen for illustration because they contain the extremes of surface temperatures for the 82 coincident radiosonde profiles examined to date. The 20 February Poker Flats profile and the 11 January Primrose Lake profile

were chosen for illustration because these profiles have the largest discrepancy between radiosonde and NEMS temperatures at 300 and at 1000 mb, respectively. Features such as the warm lower stratosphere and extremely cold lower troposphere for the 18 January Poker Flats profile, and the very cold tropopause and warm lower troposphere for the 27 June Ft. Sherman profile are clearly reproduced by the NEMS-determined profile. Features of small vertical extent such as the narrow cold feature near 300 mb in the 20 February Poker Flats profile and the sharp inversion at 1000 mb in the 11 January Primrose Lake profile are not picked up by the NEMS measurement, and give rise to the largest errors in the NEMS determinations.

When comparing the NEMS and radiosonde profiles, it must be remembered that discrepancies may also arise because the NEMS measurement is averaged over a surface area of approximately 200 km by 300 km, whereas the radiosonde measurement is a point measurement.

Results obtained from comparison of all 82 coincident radiosonde and NEMS profiles are given in Fig. 9. This figure consists of histograms which give, for seven of the standard NMC pressure levels, the distribution of 1) radiosonde variation about the mean, 2) the discrepancy between NEMS and radiosonde, 3) the discrepancy between NEMS and the interpolated NMC grid, 4) the discrepancy between the interpolated NMC grid and radiosonde, and 5) the interpolated NMC grid variation about the mean. The sample size N of the quantities involving interpolated grid data is 39 rather than 82, the number of coincident radiosondes, because the appropriate NMC data covering the times of all the radiosondes was not available at the time our analyses were performed. Also given in Fig. 9 are values for the mean m and standard deviation σ for the quantities described by the histograms. The standard deviations for these quantities are plotted in Fig. 10 as a function of altitude for the NMC levels.

The extent to which the histograms for the NEMS discrepancies are narrower than the histograms for variations about the mean indicates the extent to which the NEMS measurement improves knowledge of the temperature profile. As can be seen from Fig. 9, the improvement is significant. The reduction by NEMS of the standard deviation of the temperature profile uncertainty is clearly illustrated in Fig. 10. The *a priori* standard deviation in the temperature profile ranges from a maximum near 20 K at the surface to a minimum near 6 K at 250 and 30 mb. With the exception of the 1000 mb level where surface effects can produce sharp vertical structure not picked up by NEMS, the rms discrepancy between NEMS and radiosonde profiles varies between 2.5 and 4 K.

It will be noticed from Figs. 9 and 10 that less discrepancy exists between NEMS and the interpolated grid than between NEMS and radiosonde profiles. This may be due to the fact that both NEMS and the NMC grids have approximately the same spatial resolution, while the radiosonde measurements are point values. If so, variation in the horizontal structure of temperature over ~200 km is larger than errors introduced by time interpolation of the NMC grid.

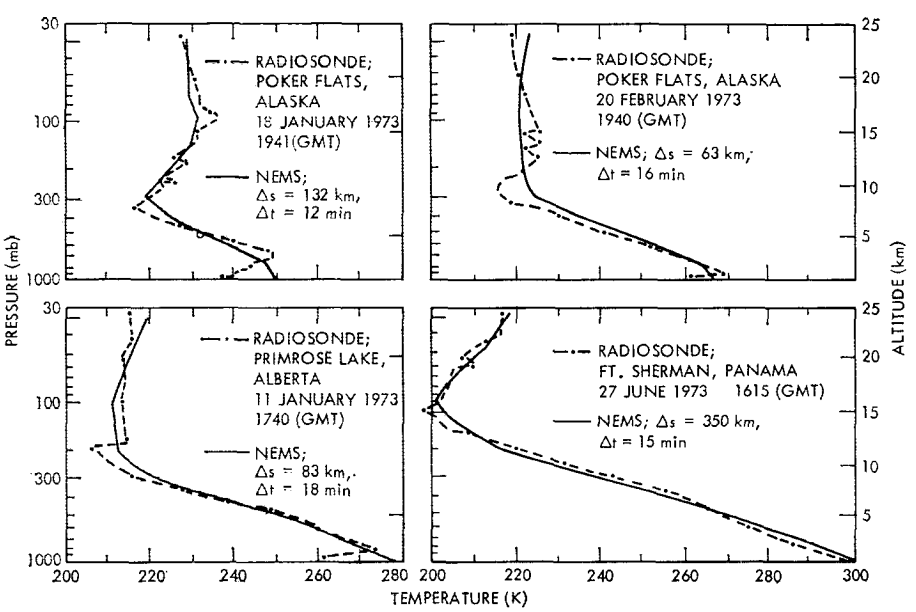

FIG. 8. Comparisons of individual temperature soundings by NEMS and coincident radiosondes. The spatial difference Δs and time difference Δt of the NEMS sounding relative to the radiosonde are indicated for each sounding.

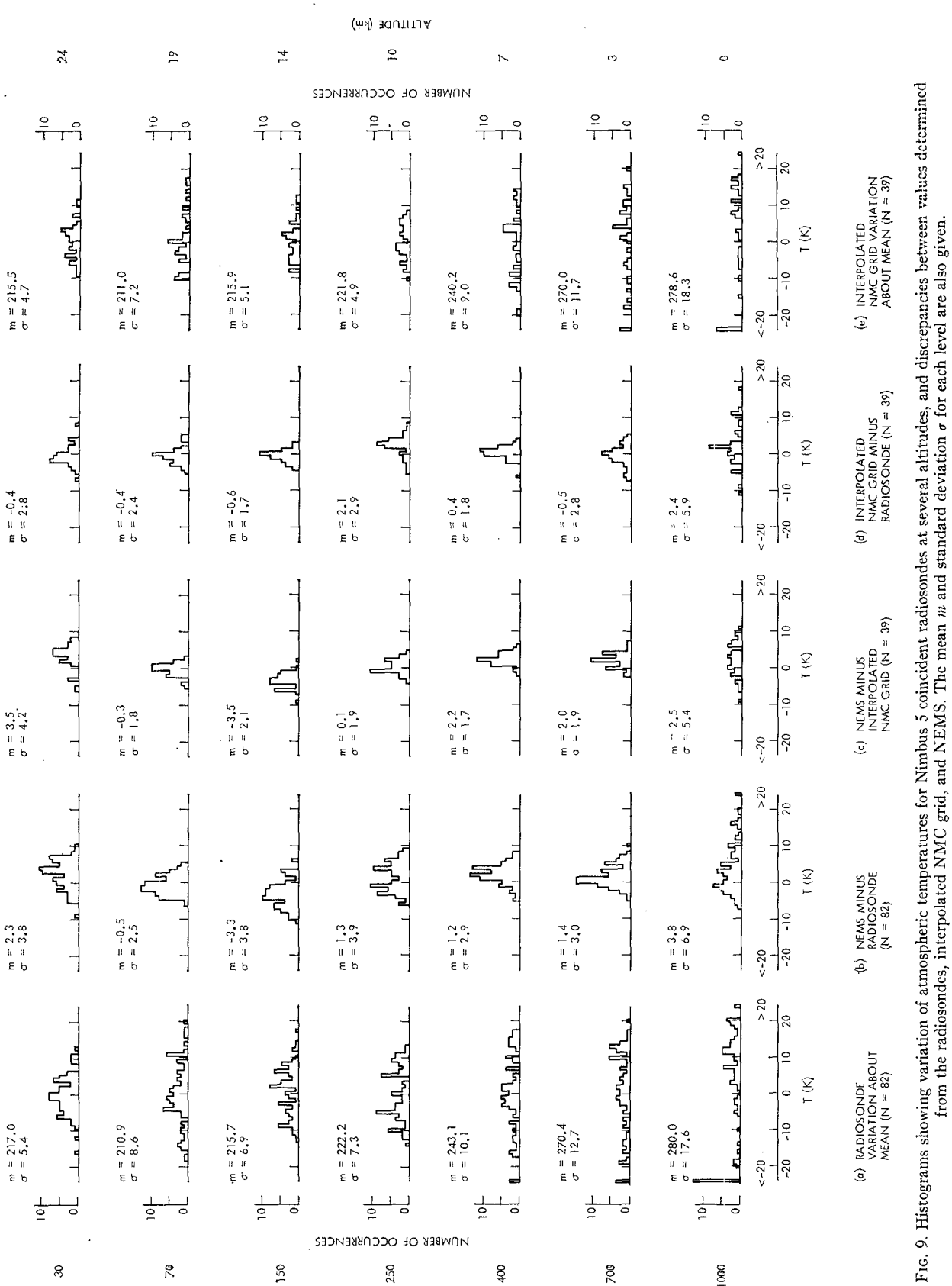

FIG. 9. Histograms showing variation of atmospheric temperatures for Nimbus 5 coincident radiosondes at several altitudes, and discrepancies between values determined from the radiosondes, interpolated NMC grid, and NEMS. The mean m and standard deviation σ for each level are also given.

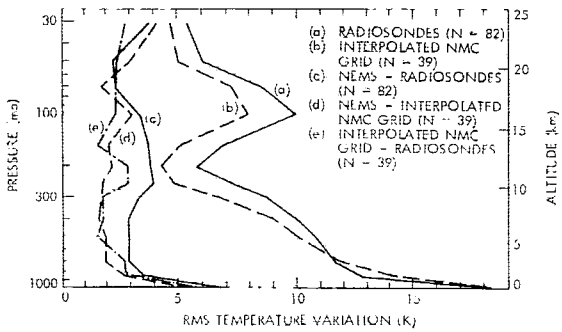

FIG. 10. Comparison of rms temperature variations and discrepancies versus altitude for the Nimbus 5 coincident radiosondes.

The discrepancy between the interpolated NMC grid and radiosonde profiles gives a rough indication of the accuracy of these comparison data. This discrepancy is seen to have rms values of between 2 and 3 K except at the surface where it is ~5 K. This is approximately the accuracy expected for NEMS, and illustrates the problem of obtaining ground-truth data for evaluating the NEMS accuracy.

It is also of interest to look at "worst case" NEMS performance to estimate the maximum errors to be expected from NEMS. This is shown in Fig. 11, which gives the maximum absolute discrepancy between NEMS and coincident radiosonde temperature measurements for each of the standard levels. Maximum discrepancies are ~10 K away from the surface and usually occur when sharp vertical structure exists in the temperature profile. Shown also in Fig. 11 is the maximum deviation of the radiosonde temperatures from the mean values, which is seen to be significantly larger than the maximum NEMS discrepancies, indicating maximum NEMS errors still provide significant information on the atmospheric temperature structure.

Figs. 12–14 give rms discrepancies between NEMS and radiosonde profiles for soundings from individual

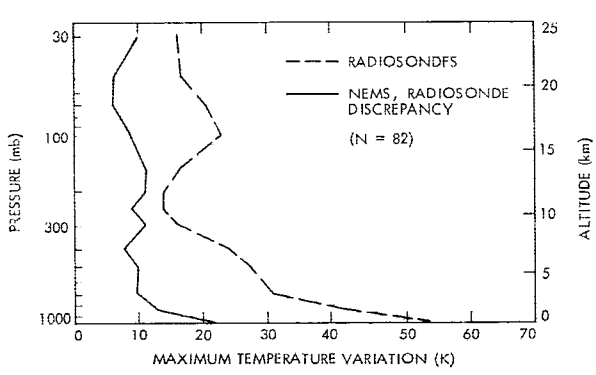

FIG. 11. Maximum temperature variations measured by Nimbus 5 coincident radiosondes, and maximum discrepancy between NEMS and radiosonde-measured temperature.

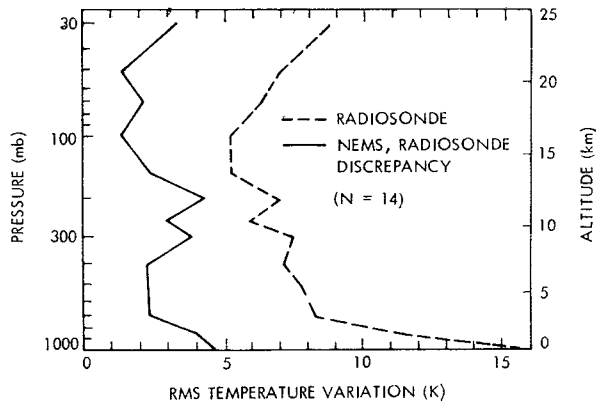

FIG. 12. Temperature variation (rms) in radiosonde measurements and rms discrepancies between radiosonde and NEMS for Ft. Churchill soundings.

radiosonde stations at Ft. Churchill, White Sands and Barking Sands. These discrepancies are 2–3 K over most of the troposphere. The *a priori* variation of the radiosonde measurements is also shown in these figures, and over most of the troposphere is 5–8 K for Ft. Churchill, 3–8 K for White Sands, and 2–4 K for Barking Sands. The rms variation at the 1000 mb level for Ft. Churchill is larger, ~16 K, and the NEMS discrepancy for this case is also somewhat larger, ~4.5 K.

Figs. 15–18 give rms discrepancies between NEMS and the interpolated NMC grid for selected regions in the Northern Hemisphere. The curves labeled DECEMBER show results of comparisons made over a period between 23 and 28 December 1972, and the curves labeled JUNE show results from a period between 23 and 26 June 1973. Also shown in these figures are the rms variation in the interpolated NMC grid profiles and the number N of soundings that were compared in each case. The NEMS discrepancies given in the figures do not include an average offset that exists for each level.

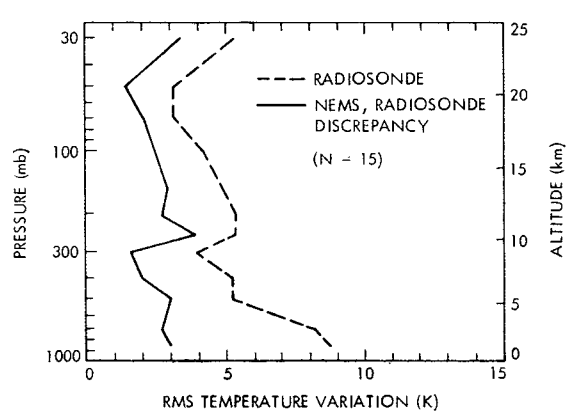

FIG. 13. As in Fig. 12 except for White Sands soundings.

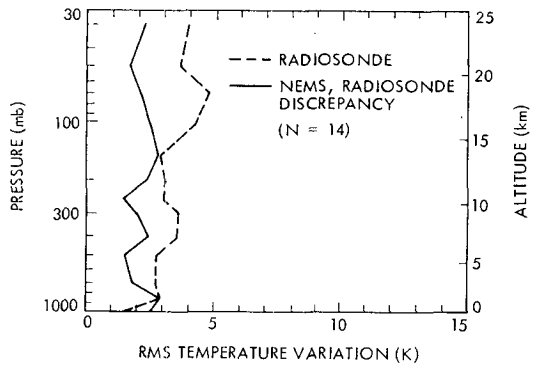

FIG. 14. As in Fig 12 except for Barking Sands soundings.

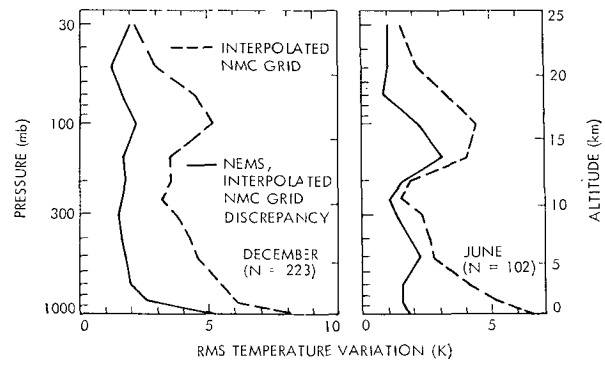

FIG. 15. Comparison of rms temperature variation from the interpolated NMC grid and the rms discrepancy between the interpolated grid and NEMS for the continental United States.

Fig. 15 shows results obtained for continental United States, not including surrounding offshore waters. This region was selected for comparison because it is where the NMC grid was considered most reliable due to the density of radiosonde stations in the United States. It must be remembered, however, that the grid, which is produced for 0000 and 1200 GMT, had to be interpolated up to 6 h in time to correspond to the times (near local noon and midnight) when Nimbus 5 was over the United States. The rms discrepancy between NEMS and the interpolated grid is 1–2 K except near the surface in December where it is near 5 K, and at 250 mb in June where it is near 3 K. These discrepancies are slightly better than the theoretical accuracy predicted in Fig. 7, probably due to the fact that the inherent variation in the temperature profile for this region is less than that for the ensemble of radiosondes used to obtain the results shown in Fig. 7.

Fig. 16 shows similar results, but for the combined four regions labeled ALASKA, EUROPE, JAPAN and UNITED STATES in Fig. 3. These regions were selected to cover a wide range of atmospheric conditions and to eliminate regions where the NMC grid is expected to be less reliable. The discrepancy between NEMS and the interpolated grid for these regions is 2–3 K except at the surface and the 70 and 50 mb levels in December. The increased discrepancies at 70 and 50 mb may be due to an inadequate amount of high-altitude data used in the computation of the **D** matrices, or they may be due to the greater time interpolation required for stratospheric variables since NMC stratospheric analysis grids are produced only once daily.

Temperature variations in the tropics are much smaller than in higher latitudes. To evaluate the performance of NEMS in tropical regions, we examined the two regions in Fig. 3 labeled TROPICAL ATLANTIC and TROPICAL PACIFIC. The results of this examination are given in Fig. 17, where comparisons in the December and June time periods have been grouped together. As can be seen, the inherent variation in the tropical temperature profile, as determined from the NMC grid, is only 1–2 K throughout the altitude region sensed by NEMS. The discrepancy between NEMS and the interpolated grid is less than the inherent variation by ~0.5 K for pressure levels between 700 and 70 mb, indicating the NEMS measurements do obtain some useful informa-

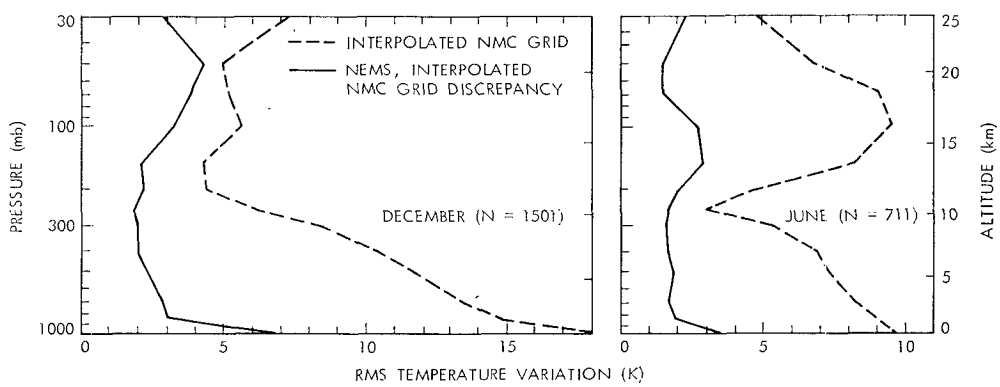

FIG. 16. Comparison of rms temperature variation from the interpolated NMC grid and the rms discrepancy between the interpolated grid and NEMS for selected verification regions of the United States, Alaska, Europe and Japan.

tion about the tropical temperature structure. An important question relating to the usefulness of the NEMS measurements in the tropics is the stability of the average "offset" between NEMS and the NMC grid. This stability is now being investigated.

Finally, the usefulness of any measurement technique depends upon how much new information, or improved accuracy, it supplies about the quantity being measured; in our case, the quantity is the atmospheric temperature profile. The difference between the inherent variation in the temperature profile and the discrepancy between NEMS and the interpolated grid is a measure of the improved accuracy NEMS supplies about the atmospheric temperature profile, over that which could be expected from climatological statistics. This improvement is shown in Figs. 18 and 19 for various regions.

Fig. 18 gives the improvement of NEMS over climatology, both with and without the average offset, between NEMS and the NMC grid, for the combined ALASKA, EUROPE, JAPAN and UNITED STATES regions shown in Fig. 3. Disregarding the average offset, the improvement at altitudes between the surface and 200 mb is 2–12 K in December and 2–7 K in June. At altitudes above 200 mb, the improvement is 1–2 K in December and 2 8 K in June. If the average offsets are not corrected for, the improvement is 1–2 K less.

Fig. 19 gives the improvement of NEMS over climatology for selected individual regions that are defined in the Northern Hemisphere map of Fig. 3. For the continental United States and northern Pacific the improvement is 1–5 K. In the tropics where the inherent variation is small, there is improvement of 0–0.5 K between 700 and 70 mb levels, but degradation (i.e., there is more discrepancy between NEMS and NMC than the inherent variation in the NMC values) outside these levels. The improvement for central Asia is 1–3 K in December and 0–3 K in June, and for Alaska the improvement is 2–3 K in December and 1–2 K in June.

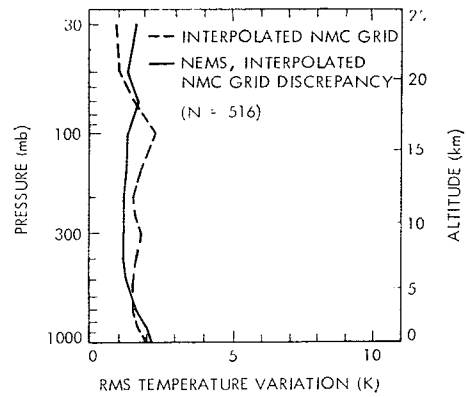

FIG. 17. Comparison of rms temperature variation from the interpolated NMC grid and the rms discrepancy between the interpolated grid and NEMS for tropical Atlantic and Pacific regions including both December and June data.

8. Conclusions

As shown in Fig. 2, the NEMS instrument can measure atmospheric temperatures averaged over the NEMS weighting function layers with an rms accuracy of a few tenths of a degree Kelvin for measurement integration times of 16 s.

The most meaningful indications of the NEMS accuracy in inferring atmospheric temperatures at the discrete levels used in the NMC operational numerical model are probably the results shown in Fig. 15. Those results were obtained from data taken over the continental United States where the NMC analysis grid, which was used for ground truth, is expected to be most reliable. The results indicate that the NEMS rms temperature uncertainty averaged over the lower thirteen NMC levels is 2.1 K in December and 1.6 K in June, with no corrections having been

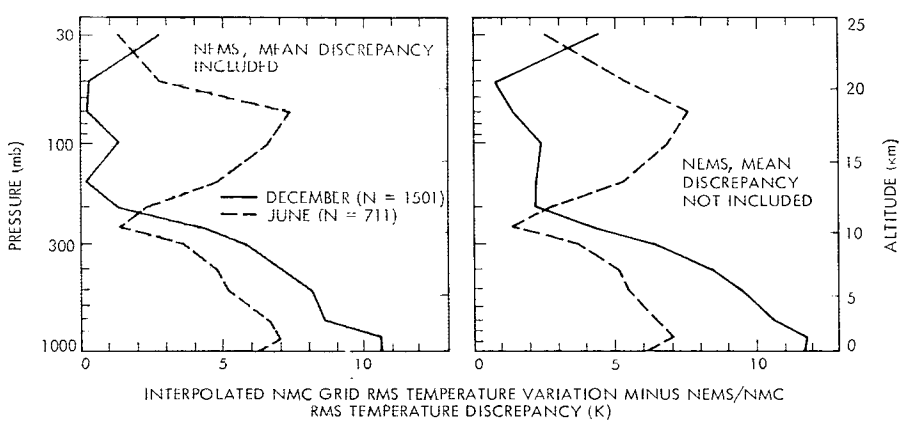

FIG. 18. Rms improvement provided by NEMS to *a priori* variation of atmospheric temperatures for combined selected verification regions.

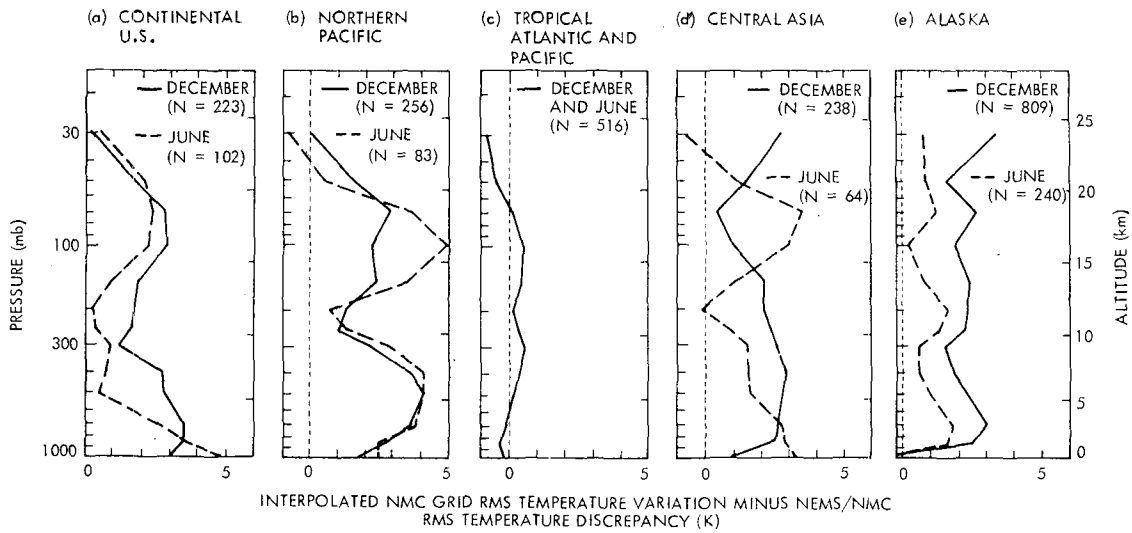

FIG. 19. Rms improvement provided by NEMS to *a priori* variation of atmospheric temperatures for individual verification regions.

made for the effects of clouds. The larger uncertainty in December is mostly due to the increased uncertainty in the 1000 mb temperature in December.

The NEMS results have demonstrated the potential of passive microwave techniques for remote sensing of atmospheric temperatures from earth orbiting satellites. We feel that these techniques will prove useful for providing initial boundary conditions for numerical weather prediction and for other fields of atmospheric sciences. Quantitative determination of the extent to which microwave measurements can improve weather forecasts will come with the use of such measurements in numerical prediction models. A microwave instrument is now being developed for such operational use on the TIROS weather satellites.

Acknowledgments. We acknowledge the assistance of NEMS co-investigators A. H. Barrett, F. T. Barath, N. E. Gaut, E. J. Johnston, W. B. Lenoir and P. W. Rosenkranz on various aspects of the experiment; J. C. Blinn III for assistance with the instrument calibration; H. M. Woolf and M. E. Gelman for assistance with the comparison radiosonde and NMC analysis data; and W. Nordberg for assistance in establishing the NEMS experimental program.

This work represents research carried out at the Jet Propulsion Laboratory, California Institute of Technology, and at the Research Laboratory of Electronics, Massachusetts Institute of Technology, under Contracts NAS 7-100 and NAS 5-21980, respectively, sponsored by the National Aeronautics and Space Administration.

REFERENCES

Artman, J. O., and J. P. Gordon, 1954: Absorption of microwaves by oxygen in the millimeter wavelength region. *Phys. Rev.*, **96**, 1237–1245.

Barnett, J. J., M. J. Cross, R. S. Harwood, J. T. Houghton, C. G. Morgan, G. E. Peckham, C. D. Rodgers, S. D. Smith and E. J. Williamson, 1972: The first year of the selective chopper radiometer on Nimbus 4. *Quart. J. Roy. Meteor. Soc.*, **98**, 17–37.

Barrett, A. H., J. W. Kuiper and W. B. Lenoir, 1966: Observations of microwave emission by molecular oxygen in the terrestrial atmosphere. *J. Geophys. Res.*, **71**, 4723–4734.

Carter, C. J., R. L. Mitchell and E. E. Reber, 1968: Oxygen absorption measurements in the lower atmosphere. *J. Geophys. Res.*, **73**, 3113–3120.

Chahine, M. T., 1968: Determination of the temperature profile in an atmosphere from its outgoing radiance. *J. Opt. Soc. Amer.*, **58**, 1634–1637.

——, 1970: Inverse problems in radiative transfer: Determination of atmospheric parameters. *J. Atmos. Sci.*, **27**, 960–967.

——, 1972: A general relaxation method for inverse solution of the full radiative transfer equation. *J. Atmos. Sci.*, **29**, 741–747.

——, 1974: Remote sounding of cloudy atmospheres, I. The single cloud layer. *J. Atmos. Sci.*, **31**, 233–243.

Conrath, B. J., 1972: Vertical resoltuion of temperature profiles obtained from remote radiation measurements. *J. Atmos. Sci.*, **29**, 1262–1271.

Crawford, A. B., and D. C. Hogg, 1956: Measurement of atmospheric attenuation at millimeter wavelengths. *Bell Sys. Tech. J.*, **35**, 907–916.

Gordon, R. G., 1967: On the pressure broadening of molecular multiplet spectra. *J. Chem. Phys.*, **46**, 448–455.

Gross, E. P., 1955: Shape of collision-broadened spectral lines. *Phys. Rev.*, **97**, 395–403.

Hanel, R. A., B. Schlachman, F. D. Clark, C. H. Prokesh, J. B. Taylor, W. M. Wilson and L. Chaney, 1970: The Nimbus III Michelson interferometer. *Appl. Opt.*, **9**, 1767–1774.

——, B. Schlachman, D. Rogers and D. Vanous, 1971: Nimbus 4 Michelson interferometer. *Appl. Opt.*, **10**, 1376–1382.

Houghton, J. T., and S. D. Smith, 1972: The selective chopper radiometer (SCR) experiment. *The Nimbus-5 User's Guide*, NASA Goddard Space Flight Center, Greenbelt, Md., 131–139.

——, and F. W. Taylor, 1973: Remote sounding from artificial satellites and space probes of the atmospheres of the earth and the planets. *Rep. Prog. Phys.*, **36**, 827–919.

Jastrow, R., and M. Halem, 1973: Accuracy and coverage of temperature data derived from the IR radiometer on the NOAA 2 satellite. *J. Atmos. Sci.*, **30**, 958 964.

Kaplan, L. D., 1959: Inference of atmospheric structure from remote radiation measurements. *J. Opt. Soc. Amer.*, **49**, 1004–1007.

Kennedy, J. S., and W. Nordberg, 1967: Circulation features of the stratosphere derived from radiometric temperature measurements with the TIROS-7 satellite. *J. Atmos. Sci.*, **24**, 711–719.

King, J. I. F., 1956: The radiative heat transfer of Planet Earth. *Scientific Uses of Earth Satellites*, University of Michigan Press, 133-136.

Lenoir, W. B., 1968: Microwave spectrum of molecular oxygen in the mesosphere. *J. Geophys. Res.*, **73**, 361–376.

——, J. W. Barrett and D. C. Papa, 1968: Observations of microwave emission by molecular oxygen in the stratosphere. *J. Geophys. Res.*, **73**, 1119–1126.

Malkevich, M. S., V. P. Kozlov and I. A. Gorchakova, 1969: On application of the statistical method for determination of atmospheric temperature profiles from satellites. *Tellus*, **21**, 389–394.

Meeks, M. L., 1961: Atmospheric emission and opacity at millimeter wavelengths due to oxygen. *J. Geophys. Res.*, **66**, 3749–3757.

——, and A. E. Lilley, 1963: The microwave spectrum of oxygen in the eath's atmosphere. *J. Geophys. Res.*, **68**, 1683–1703.

Miner, G. F., D. D. Thornton and W. J. Welch, 1972: The inference of atmospheric temperature profiles from ground-based measurements of microwave emission from atmospheric oxygen. *J. Geophys. Res.*, **77**, 975–991.

Pokrovsky, O. M., 1972: Comparison of methods of solution of inverse problems in atmospheric optics. *Izv. Akad. Nauk SSSR, Fiz. Atmos. Okean.*, **8**, 231–233.

——, and Yu M. Timofeyev, 1972: A general statistical approach for solution of inverse problems of atmospheric optics. *Meteor. Gidrol.*, **1**, 52 59.

Poon, R. K. L., 1974: Atmospheric opacity near half centimeter wavelength. Sc.D. thesis, M.I.T., Cambridge, Mass.

Reber, E. E., 1972: Absorption of the 4- to 6-millimeter wavelength band in the atmosphere. *J. Geophys. Res.*, **77**, 3831–3845.

Rodgers, C. D., 1966: Satellite infrared radiometer. A discussion of inversion methods. Clarendon Laboratory, Memo. No. 66.13, University of Oxford.

, 1970: Remote sounding of the atmospheric temperature profile in the presence of cloud. *Quart. J. Roy. Meteor. Soc.*, **96**, 654–666.

, 1971: Some theoretical aspects of remote sounding in the earth's atmosphere. *J. Quant. Spectrosc. Radiat. Transfer*, **11**, 767–777.

Rosenkranz, P. W., 1975: Shape of the 5-mm oxygen band in the atmosphere. *IEEE Trans. Ant. Prop.*, **AP-23**, 498–506.

, F. T. Barath, J. C. Blinn III, E. J. Johnston, W. B. Lenoir, D. H. Staelin and J. W. Waters, 1972: Microwave radiometric measurements of atmospheric temperature and water from an aircraft. *J. Geophys. Res.*, **77**, 5833–5844.

Schulze, A. E., and C. W. Tolbert, 1963: Shape, intensity, and pressure broadening of the 2.53 millimetre wave-length oxygen absorption line. *Nature*, **200**, 747–750.

Smith, W. L., H. M. Woolf and W. J. Jacob, 1970. A regression method for obtaining real-time temperature and geopotential height profiles from satellite spectrometer measurements and its application to Nimbus 3 SIRS observations. *Mon. Wea. Rev.*, **98**, 582–603.

——, H. B. Howell, J. C. Fischer, M. C. Chalfant and D. T. Hilleary, 1972a: The infrared temperature profile radiometer (ITPR) experiment. *The Nimbus-5 User's Guide*, NASA Goddard Space Flight Center, Greenbelt, Md., 107–130.

——, H. M. Woolf and H. E. Fleming, 1972b: Retrieval of atmospheric temperature profiles from satellite measurements for dynamical forecasting. *J. Appl. Meteor.*, **11**, 113–122.

Staelin, D. H., 1966: Measurements and interpretation of the microwave spectrum of the terrestrial atmosphere near 1-centimeter wavelength. *J. Geophys. Res.*, **71**, 2875–2881.

——, 1969: Passive remote sensing at microwave wavelengths. *Proc. IEEE*, **57**, 427–439.

——, A. H. Barrett, J. W. Waters, F. T. Barath, E. J. Johnston, P. W. Rosenkranz, N. E. Gaut and W. B. Lenoir, 1973: Microwave spectrometer on the Nimbus 5 satellite: Meteorological and geophysical data. *Science*, **182**, 1339–1341.

——, A. L. Cassel, K. F. Kunzi, R. L. Pettyjohn, R. K. L. Poon, P. W. Rosenkranz and J. W. Waters, 1975a. Microwave atmospheric temperature sounding: Effects of clouds on the Nimbus 5 satellite data. *J. Atmos. Sci.*, **32**, 1970–1976.

——, K. F. Kunzi, R. L. Pettyjohn, P. W. Rosenkranz and J. W. Waters, 1975b: Remote sensing of atmospheric liquid water and water vapor content with the Nimbus 5 microwave spectrometer. To be submitted to *J. Atmos. Sci.*

Straiton, A. W., and C. W. Tolbert, 1960: Anomalies in the absorption of radio waves by atmospheric gases. *Proc. IRE*, **48**, 898–903.

Tomiyasu, K., 1974: Remote sensing of the Earth by microwaves. *Proc. IEEE*, **62**, 86-92.

Twomey, S., 1965: The application of numerical filtering to the solution of integral equations encountered in indirect sensing measurements. *J. Franklin Inst.*, **279**, 95–109.

Van Vleck, J. H., 1947: The absorption of microwaves by O_2. *Phys. Rev.*, **71**, 413–424.

Wark, D. Q., and D. T. Hilleary, 1969: Atmospheric temperature: Successful test of remote probing. *Science*, **165**, 1256–1258.

Waters, J. W., 1973: Ground-based measurement of millimetre-wavelength emission by upper stratospheric O_2. *Nature*, **242**, 506–508.

Westwater, E. R., 1972: Ground-based determination of low-altitude temperature profiles by microwaves. *Mon. Wea. Rev.*, **100**, 15–29.

——, and O. N. Strand, 1968: Statistical estimation of the numerical solution of a Fredholm integral equation of the first kind. *J. Assoc. Comput. Mach.*, **15**, 100–114.

Zhevakin, S. A., and A. P. Naumov, 1963: Coefficient of absorption of electromagnetic waves by water vapor in the range 10 μ–2 cm. *Izv. Vyssh. Uchebn. Zaved. Radiofiz.*, **6**, 674–694.